



Swimming and pumping of rigid helical bodies in viscous fluids

Lei Li and Saverio E. Spagnolie

Citation: [Physics of Fluids \(1994-present\)](#) **26**, 041901 (2014); doi: 10.1063/1.4871084

View online: <http://dx.doi.org/10.1063/1.4871084>

View Table of Contents: <http://scitation.aip.org/content/aip/journal/pof2/26/4?ver=pdfcov>

Published by the [AIP Publishing](#)

Articles you may be interested in

[Two regimes of self-propelled motion of a torus rotating about its centerline in a viscous incompressible fluid at intermediate Reynolds numbers](#)

Phys. Fluids **24**, 053603 (2012); 10.1063/1.4717760

[Nonlinear viscous fluid patterns in a thin rotating spherical domain and applications](#)

Phys. Fluids **23**, 123102 (2011); 10.1063/1.3665132

[Microfluidic four-roll mill for all flow types](#)

Appl. Phys. Lett. **90**, 074103 (2007); 10.1063/1.2472528

[Fluid pumped by magnetic stress](#)

Appl. Phys. Lett. **86**, 024102 (2005); 10.1063/1.1846956

[Molecular transition and slip flows in rotating helical channels of drag pump](#)

AIP Conf. Proc. **585**, 893 (2001); 10.1063/1.1407653



Re-register for Table of Content Alerts

Create a profile.



Sign up today!



Swimming and pumping of rigid helical bodies in viscous fluids

Lei Li^{a)} and Saverio E. Spagnolie^{b)}

Department of Mathematics, University of Wisconsin-Madison, 480 Lincoln Dr., Madison, Wisconsin 53706, USA

(Received 18 January 2014; accepted 27 March 2014; published online 21 April 2014)

Rotating helical bodies of arbitrary cross-sectional profile and infinite length are explored as they swim through or transport a viscous fluid. The Stokes equations are studied in a helical coordinate system, and closed form analytical expressions for the force-free swimming speed and torque are derived in the asymptotic regime of nearly cylindrical bodies. High-order accurate expressions for the velocity field and swimming speed are derived for helical bodies of finite pitch angle through a double series expansion. The analytical predictions match well with the results of full numerical simulations, and accurately predict the optimal pitch angle for a given cross-sectional profile. This work may improve the modeling and design of helical structures used in microfluidic manipulation, synthetic microswimmer engineering, and the transport and mixing of viscous fluids. © 2014 AIP Publishing LLC. [<http://dx.doi.org/10.1063/1.4871084>]

I. INTRODUCTION

The transport of fluid by helical structures has a long history in engineering, dating as far back as the invention of the screw pump by Archimedes in ancient Greece.¹ Today, helically driven viscous flows are of central importance in such applications as the mixing of Newtonian²⁻⁵ and complex⁶ fluids. Helical flows can lead to chaotic mixing patterns, which may allow for efficient mixing even in highly dissipative systems.⁷ There have also been a number of recent bio-inspired feats of engineering, including the development of chiral magnetic bodies that may be propelled through viscous environments by magnetic fields.⁸⁻¹² Peyer *et al.*¹³ give a review of recent applications using magnetic helical structures at the micrometer scale, which among other exciting uses may someday lead to minimally invasive surgery and drug delivery techniques.¹⁴⁻¹⁶

A rather older example of helical fluid transport is found in the bacterial flagellum, which microorganisms have used to propel themselves through fluids for over two billion years.¹⁷⁻¹⁹ The fluid flow driven by the motion of an immersed body is characterized by the Reynolds number, $Re = \rho UL/\mu$, where U and L are characteristic velocity and length scales, ρ is the fluid density, and μ is the fluid viscosity. Low Reynolds number flows are those in which viscous dissipation dominates inertial effects. A serious constraint for swimming and pumping in viscous fluids is the Scallop Theorem, which states that no time-reversible boundary motion may lead to either swimming or net transport at zero Reynolds number.²⁰ To overcome this challenge, many microorganisms (for which the flow is characterized by $Re \approx 10^{-4} - 10^{-2}$) evolved to swim through fluids by rotating one or many helical flagella. The drag anisotropy of filaments in viscous fluids, along with the unidirectional passage of waves along the flagellum, leads to a net transport of the organism.^{17,21,22} Recent theoretical and numerical works have investigated the validity of theoretical approximations,²³ synchronization, and bundling of multiple helical filaments,²⁴⁻³² and the locomotion of helical

^{a)}leili@math.wisc.edu

^{b)}spagnolie@math.wisc.edu

bodies in complex fluid environments.^{33–37} A review of the large body of related literature has been provided by Lauga and Powers.¹⁸

A natural question in the study of either biological or engineered propulsion and pumping is that of optimization. Inspired by the pioneering work on the subject by Lighthill,¹⁷ there have been many recent studies of optimal helical geometries for propulsion in viscous fluids. Investigations have included the hydrodynamic optimization of: helical waveforms for propelling a spherical load,³⁸ general helical propellers,³⁹ polymorphic forms in the bacterial flagellum,^{40,41} and helical bodies in a cylindrical channel.⁴² A thermodynamic efficiency for Stokesian swimming has also been introduced.⁴³ Numerical optimization has been performed for chiral colloidal aggregates and cargo-bearing bodies,^{44,45} and analytical optimization has been considered for slender magnetically driven filaments using a local resistive force theory.⁴⁶

In this paper, we investigate the force-free swimming of an infinitely long, rotating helical body of a given arbitrary cross-section in an infinite fluid. Helical coordinates are adopted to study the Stokes equations in a body-conforming coordinate system. Closed form analytical expressions for the force-free swimming speed and torque are derived in the asymptotic regime of nearly cylindrical bodies. The analytical predictions match well with the results of full numerical simulations, and accurately predict the optimal pitch angle for a given cross-sectional profile. While we will discuss the results in the context of force-free swimming, the problems of fluid pumping and force-free swimming are simply related by a Galilean transformation. Due to the linearity of Stokes flow, the limiting far-field fluid velocity in the former may be viewed as the force-free swimming speed in the latter, and both problems are analyzed using an identical framework. In other words, although we will solve the force-free swimming problem, in so doing we will also have solved the pumping problem.

The paper is organized as follows. The equations of motion are presented and written in terms of a helical coordinate system in Sec. II. The numerical method used to study the dynamics of an arbitrary (e.g., large amplitude) body shape is described in Sec. III, which provides a basis of comparison for the asymptotic results. In Sec. IV, helical perturbations of the cylindrical base shape are studied, with resultant swimming speeds reported up to $O(\varepsilon^2)$ in the general setting, with ε the size of the relative perturbation of the cylindrical cross-sectional (circular) profile. For single Fourier-mode descriptions of the body's cross-sectional profile, we report swimming speeds accurate to $O(\varepsilon^4)$, which reveals an optimal choice of pitch angle as a function of the cross-sectional wave number, as described in Sec. V. We conclude with a discussion in Sec. VI.

II. EQUATIONS OF MOTION AND HELICAL COORDINATE SYSTEM

Consider a right-handed helical body of infinite length, rotating with angular speed ω and translating with speed U^* , immersed in a fluid of infinite extent. The surface of the body at time t is described by

$$\mathbf{y}(\theta, \zeta, t) = A \rho(\theta) [\cos(v^* \zeta + \omega t + \theta) \hat{\mathbf{x}} + \sin(v^* \zeta + \omega t + \theta) \hat{\mathbf{y}}] + (\zeta + U^* t) \hat{\mathbf{z}}, \quad (1)$$

where $\theta \in [0, 2\pi)$ and $\zeta \in (-\infty, \infty)$, and the wavelength of the deformation along the surface is given by $2\pi/v^*$ (the pitch angle is $\beta = \tan^{-1}(v^*A)$). The entire body surface is therefore set by the cross-sectional profile, $A \rho(\theta)$, and the parameter v^* , as illustrated in Fig. 1. In anticipation of studying perturbations from a cylindrical surface, we write $A \rho(\theta) = A[1 + \varepsilon f(\theta)]$, where $\rho(\theta)$, ε , and $f(\theta)$ are dimensionless, and $\rho(\theta)$ and $f(\theta)$ are periodic on $\theta \in [0, 2\pi)$. Figures 2(a)–2(c) show three examples of such bodies with cross-sectional profiles of increasing wavenumber, all with $v^*A = 1$. The fourth example in Fig. 2(d) is a right-handed helix with a left-handed surface pattern, which cannot be described by Eq. (1) but will be discussed later.

A particularly useful frame is the one in which the helical geometry (though not the material surface) remains fixed, namely, $\tilde{\mathbf{y}} = \mathbf{y} - (U^* - \omega/v^*) t \hat{\mathbf{z}}$. The new frame is unchanged from the lab frame when $U^* = \omega/v^*$. Rewriting Eq. (1) in this new frame, and defining $\tilde{\zeta} = \zeta + (\omega/v^*)t$, the body surface is described by

$$\tilde{\mathbf{y}}(\theta, \tilde{\zeta}) = A(1 + \varepsilon f(\theta)) [\cos(v^* \tilde{\zeta} + \theta) \hat{\mathbf{x}} + \sin(v^* \tilde{\zeta} + \theta) \hat{\mathbf{y}}] + \tilde{\zeta} \hat{\mathbf{z}}, \quad (2)$$

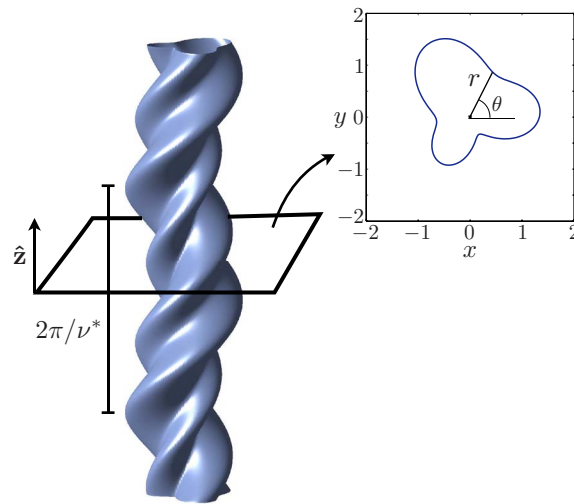


FIG. 1. The surface of a general helical body is described by the cross-sectional parameterization $A \rho(\theta) = A(1 + \varepsilon f(\theta))$ and the vertical pitch by $2\pi/\nu^*$ (the pitch angle is given by $\beta = \tan^{-1}(\nu^*A)$). The example shown has a cross-sectional profile $\rho(\theta) = 1 + (1/3)(\sin(\theta) - \cos(3\theta))$. A polar coordinate system is defined on a planar cross-section as shown.

while the material on the helical surface moves with velocity

$$\frac{\partial}{\partial t} \tilde{\mathbf{y}}(\theta, \tilde{\zeta}(\zeta, t)) = \omega A(1 + \varepsilon f(\theta)) [-\sin(\nu^* \tilde{\zeta} + \theta) \hat{\mathbf{x}} + \cos(\nu^* \tilde{\zeta} + \theta) \hat{\mathbf{y}}] + \frac{\omega}{\nu^*} \hat{\mathbf{z}}. \quad (3)$$

The equations describing a Newtonian fluid flow at zero Reynolds number are the Stokes equations, which are Galilean invariant and so are unchanged in a frame moving with constant velocity. The incompressible Stokes equations in the moving frame described above are given by

$$\nabla \cdot \boldsymbol{\sigma} = -\nabla p + \mu \Delta \mathbf{u} = \mathbf{0}, \quad (4)$$

$$\nabla \cdot \mathbf{u} = 0, \quad (5)$$

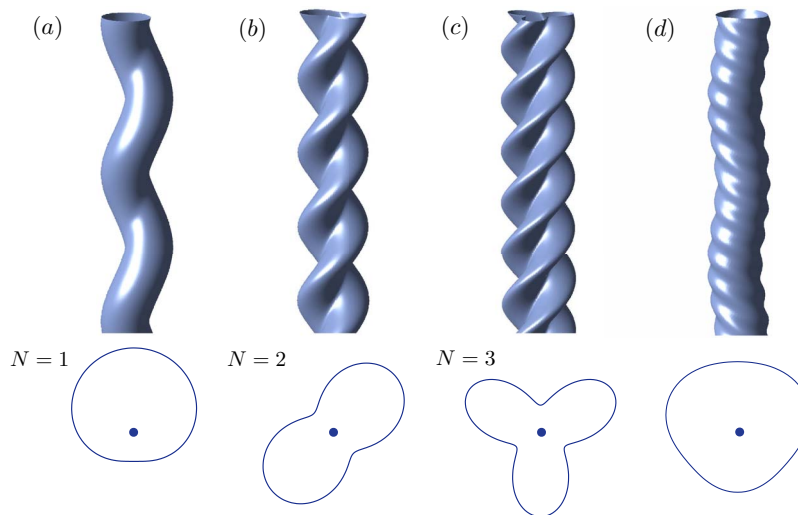


FIG. 2. Helical body examples with $\nu = 1$, with cross-section parameterizations given by: (a) $\rho(\theta) = 1 + (1/2)\sin(\theta)$; (b) $\rho(\theta) = 1 + (1/2)\sin(2\theta)$; (c) $\rho(\theta) = 1 + (1/2)\sin(3\theta)$. (d) A right-handed helix with a left-handed helical surface pattern, selected such that the swimming speed during rotation is approximately zero. Cross-sections in the $z = 0$ plane are also shown.

where $\boldsymbol{\sigma} = -p\mathbf{I} + 2\mu\mathbf{E}$ is the Newtonian fluid stress, p is the pressure, \mathbf{u} is the fluid velocity in the moving frame, $\mathbf{E} = (\nabla\mathbf{u} + \nabla\mathbf{u}^T)/2$ is the symmetric rate-of-strain tensor, and μ is the viscosity. The fluid velocity in the lab frame is given by $\mathbf{u}_{lab} = \mathbf{u} + (U^* - \omega/\nu^*)\hat{\mathbf{z}}$. The boundary conditions are no-slip on the helical surface, denoted by ∂S , and decay of the velocity in the lab frame as $\hat{\mathbf{z}} \times \mathbf{y} \rightarrow \infty$, so that at a point $\tilde{\mathbf{x}}$ in the moving frame we have

$$\mathbf{u}(\tilde{\mathbf{x}} \in \partial S, t) = \frac{\partial \tilde{\mathbf{y}}}{\partial t}, \quad \mathbf{u}(\hat{\mathbf{z}} \times \tilde{\mathbf{x}} \rightarrow \infty, t) = \left(\frac{\omega}{\nu^*} - U^*\right)\hat{\mathbf{z}}. \quad (6)$$

We will consider the problem of swimming with zero net force (see Ref. 18), an assumption that closes the system. In the new frame, the Stokes equations (4) and (5), the boundary description (2), and the boundary conditions (6) are independent of time, and correspond to a steady state solution of the swimming speed and fluid velocity. It is therefore sufficient to solve the equations of motion at $t = 0$, when the new moving frame is identical to the lab frame, $\tilde{\zeta} = \zeta$ and $\tilde{\mathbf{y}} = \mathbf{y}$.

The system is made dimensionless by scaling lengths by A , time by $1/\omega$, velocities by $A\omega$, and stresses by $\mu\omega$. The dimensionless swimming speed is written as $U = U^*/(A\omega)$, and we define $\nu = \nu^*A$. Understanding all variables henceforth to be dimensionless, the material velocity on the body surface is described in the moving frame (see Eq. (3)) by

$$\frac{\partial}{\partial t}\tilde{\mathbf{y}}(\theta, \tilde{\zeta}(\zeta, t)) = (1 + \varepsilon f(\theta))[-\sin(\nu\tilde{\zeta} + \theta)\hat{\mathbf{x}} + \cos(\nu\tilde{\zeta} + \theta)\hat{\mathbf{y}}] + \frac{1}{\nu}\hat{\mathbf{z}}, \quad (7)$$

and the Stokes equations are given by $-\nabla p + \Delta\mathbf{u} = \mathbf{0}$, $\nabla \cdot \mathbf{u} = 0$.

At $t = 0$, a body conforming helical coordinate system (r, θ, ζ) is defined implicitly by

$$\mathbf{x}(r, \theta, \zeta) = r[\cos(\nu\zeta + \theta)\hat{\mathbf{x}} + \sin(\nu\zeta + \theta)\hat{\mathbf{y}}] + \zeta\hat{\mathbf{z}}, \quad (8)$$

where $\theta \in [0, 2\pi)$, $\zeta \in (-\infty, \infty)$, and $r \in [1 + \varepsilon f(\theta), \infty)$. However, we retain the convenience of orthogonality by choosing as a basis that of a cylindrical coordinate system, $(\hat{\mathbf{r}}, \hat{\boldsymbol{\theta}}, \hat{\mathbf{z}})$, with

$$\hat{\mathbf{r}} = \cos(\nu\zeta + \theta)\hat{\mathbf{x}} + \sin(\nu\zeta + \theta)\hat{\mathbf{y}}, \quad \hat{\boldsymbol{\theta}} = -\sin(\nu\zeta + \theta)\hat{\mathbf{x}} + \cos(\nu\zeta + \theta)\hat{\mathbf{y}}, \quad (9)$$

so that the nabla operator may be expressed as

$$\nabla = \hat{\mathbf{r}}\frac{\partial}{\partial r} + \hat{\boldsymbol{\theta}}\frac{1}{r}\frac{\partial}{\partial \theta} + \hat{\mathbf{z}}\left(\frac{\partial}{\partial \zeta} - \nu\frac{\partial}{\partial \theta}\right). \quad (10)$$

Taking advantage of helical symmetry, the velocity field may be written as

$$\mathbf{u}(r, \theta, \zeta) = u(r, \theta)\hat{\mathbf{r}} + v(r, \theta)\hat{\boldsymbol{\theta}} + w(r, \theta)\hat{\mathbf{z}}. \quad (11)$$

Transformation of the Stokes equations, Eqs. (4) and (5), into the helical coordinate system results in the following system:

$$\frac{\partial p}{\partial r} = \frac{1}{r}\frac{\partial}{\partial r}\left(r\frac{\partial u}{\partial r}\right) - \frac{u}{r^2} - \frac{2}{r^2}\frac{\partial v}{\partial \theta} + \frac{1}{r^2}\frac{\partial^2 u}{\partial \theta^2} + \nu^2\frac{\partial^2 u}{\partial \theta^2}, \quad (12)$$

$$\frac{1}{r}\frac{\partial p}{\partial \theta} = \frac{1}{r}\frac{\partial}{\partial r}\left(r\frac{\partial v}{\partial r}\right) - \frac{v}{r^2} + \frac{2}{r^2}\frac{\partial u}{\partial \theta} + \frac{1}{r^2}\frac{\partial^2 v}{\partial \theta^2} + \nu^2\frac{\partial^2 v}{\partial \theta^2}, \quad (13)$$

$$-\nu\frac{\partial p}{\partial \theta} = \frac{1}{r}\frac{\partial}{\partial r}\left(r\frac{\partial w}{\partial r}\right) + \frac{1}{r^2}\frac{\partial^2 w}{\partial \theta^2} + \nu^2\frac{\partial^2 w}{\partial \theta^2}, \quad (14)$$

$$\frac{\partial u}{\partial r} + \frac{u}{r} + \frac{1}{r}\frac{\partial v}{\partial \theta} - \nu\frac{\partial w}{\partial \theta} = 0. \quad (15)$$

The boundary conditions, Eqs. (6), in dimensionless form and in the helical coordinate system, are given by

$$u(r = 1 + \varepsilon f(\theta), \theta) = 0, \quad v(r = 1 + \varepsilon f(\theta), \theta) = 1 + \varepsilon f(\theta), \quad w(r = 1 + \varepsilon f(\theta), \theta) = \frac{1}{\nu}, \quad (16)$$

$$u(r \rightarrow \infty, \theta) = 0, \quad v(r \rightarrow \infty, \theta) = 0, \quad w(r \rightarrow \infty, \theta) = \frac{1}{\nu} - U. \quad (17)$$

The pressure limits to a constant value, p_∞ , as $r \rightarrow \infty$. Before solving the equations above, we first describe a numerical method for computing solutions to the full Stokes equations, which can then be used as a basis for comparison when we derive asymptotically accurate analytical solutions to the system above in Sec. IV.

III. NUMERICAL SOLUTION OF THE STOKES EQUATIONS IN A HELICAL GEOMETRY

We now describe a numerical method of solving the Stokes equations for arbitrary rotating and translating helical bodies. Once again we make use of the helical symmetry in the system, now to significantly improve the speed and accuracy of our computations. The numerical approach is based on the second kind boundary integral formulation of the Stokes equations (see Refs. 47 and 48). We solve for the mobility of a helical body with a finite number of wavelengths, N_W , and then increase N_W until further increases have negligible consequences on the computed swimming speed and torque. The dimensionless fluid velocity at a point \mathbf{x} in the fluid (in the lab frame) may be represented as an integration over the immersed boundary ∂S and the body centerline C ,

$$\mathbf{u}_{lab}(\mathbf{x}) = \int_{\partial S} \mathbf{q}(\mathbf{y}) \cdot \mathbf{T}(\mathbf{x}, \mathbf{y}) \cdot \hat{\mathbf{n}}(\mathbf{y}) dS_y + \frac{1}{8\pi} \int_C \mathbf{G}^c(\mathbf{x}, \zeta) \cdot (L \hat{\mathbf{z}}) d\zeta. \quad (18)$$

Here, $\mathbf{y} = \mathbf{y}(\theta, \zeta)$ is a parameterization of the surface, dS_y is the surface area element with respect to the integration variable \mathbf{y} , $T_{ijk}(\mathbf{x}, \mathbf{y}) = -6(x_i - y_i)(x_j - y_j)(x_k - y_k)/|\mathbf{x} - \mathbf{y}|^5$ is the Stresslet singularity, $G^c(\mathbf{x}, \zeta)_{ij} = \epsilon_{ijk}(x_k - \zeta \delta_{k3})/|\mathbf{x} - \mathbf{y}|^3$ is the rotlet (or couplet) singularity, L is an external torque per unit length acting on the body, and $\mathbf{q}(\mathbf{y})$ is an unknown density. Finally, ϵ_{ijk} is the Levi-Civita symbol, and δ_{ij} is the Kronecker delta. Flows associated with external forces and torques on the body do not lie in the range of the first integral operator above; the inclusion of singular solutions to the Stokes equations internal to the body boundary is one method of completing the flow.^{47,48} The line distribution of rotlet singularities along the helical centerline provides for a net torque and accompanying rotation of the body; since no other forms of completion are included, any flow represented by the boundary integral equation above is assured to be one in which the body experiences zero net force.

In the limit as the point \mathbf{x} is taken to a point \mathbf{x}_0 on the boundary, the no-slip boundary condition reveals an equation for the unknown density \mathbf{q} . Anticipating the relaxation of the finite helix length assumption, the rigid body velocity on the boundary at a point \mathbf{x}_0 will be written as $U \hat{\mathbf{z}} + \hat{\mathbf{z}} \times \mathbf{x}$, and after some manipulation Eq. (18) will tend to the form

$$U \hat{\mathbf{z}} + \hat{\mathbf{z}} \times \mathbf{x} = \int_{\partial S} (\mathbf{q}(\mathbf{y}) - \mathbf{q}(\mathbf{x}_0)) \cdot \mathbf{T}(\mathbf{x}_0, \mathbf{y}) \cdot \hat{\mathbf{n}}(\mathbf{y}) dS_y + \frac{1}{8\pi} \int_C \mathbf{G}^c(\mathbf{x}_0, \zeta) \cdot (L \hat{\mathbf{z}}) d\zeta. \quad (19)$$

Further investigation of the integral operator leads to the relations

$$-\frac{4\pi}{S_A} \int_{\partial S} \mathbf{q}(\mathbf{x}) dS_x = U \hat{\mathbf{z}}, \quad -4\pi \sum_{m=1}^3 \frac{1}{A_m} \mathbf{e}_m \left(\mathbf{e}_m \cdot \int_{\partial S} \mathbf{x} \times \mathbf{q}(\mathbf{x}) dS_x \right) = \hat{\mathbf{z}}, \quad (20)$$

where S_A is the surface area, $A_m = \int_{\partial S} |\mathbf{e}_m \times \mathbf{x}|^2 dS_x$, and \mathbf{e}_m is the m th Cartesian unit vector (see Ref. 48). Equations (19) and (20) form a closed system for \mathbf{q} , U , and L .

We are now set to exploit the helical symmetry in the problem of present interest. Specifically, in the event that the helical surface is of infinite length, then the density everywhere along the surface $\mathbf{y}(\theta, \zeta)$ (from Eq. (1) at $t = 0$) is given by a rotation,

$$\mathbf{q}(\mathbf{y}(\theta, \zeta)) = \mathbf{R}(\zeta; \nu) \mathbf{q}_0(\theta), \quad (21)$$

$$\mathbf{R}(\zeta; \nu) = \begin{pmatrix} \cos(\nu\zeta) & -\sin(\nu\zeta) & 0 \\ \sin(\nu\zeta) & \cos(\nu\zeta) & 0 \\ 0 & 0 & 1 \end{pmatrix}, \quad (22)$$

where $\mathbf{q}_0(\theta) = \mathbf{q}(\mathbf{y}(\theta, \zeta = 0))$. The angle θ is discretized uniformly on $[0, 2\pi)$ by setting $\theta_j = 2\pi(j-1)/M$ for $j \in \{1, \dots, M\}$. A Nyström collocation method is employed (see Ref. 49) in which the integral equation (19) is assumed to hold at the same nodes, $\mathbf{x}_0 = \mathbf{y}(\theta_j, \zeta = 0)$. This produces a linear system of equations for the density at the nodes $\mathbf{q}_0(\theta_j)$, the swimming speed U , and the torque per unit length, L . The surface integrals in Eqs. (19) and (20) are performed by truncating the surface at a finite number of wavelengths, N_W , and discretizing $\zeta \in [-N_W\pi/\nu, N_W\pi/\nu]$ at the points corresponding to the Gaussian quadrature nodes, ζ_j , with $j = 1, \dots, N_W$.

Integrals in θ and ζ are performed using Gaussian quadrature,⁵⁰ where the density \mathbf{q} is interpolated using a Fourier basis to access its values at the Gaussian quadrature nodes; equivalently, the Fourier coefficients of \mathbf{q} are taken as the unknown components of the singularity density in the linear system described above. The number of azimuthal gridpoints, M , the number of axial gridpoints, N_A , and the number of wavelengths, N_W , are chosen so that further increases change the resulting velocities and torques by less than 0.5% in every case considered. The results of a convergence study using the helical shape shown in Fig. 1 as a test case are included as Appendix A. Though they will not be needed here, the pointwise stress can also be computed from the framework of Fredholm second-kind integral equations using the Lorentz reciprocal theorem⁵¹ or by evaluating a hypersingular integral.⁵² Helical symmetry was recently exploited in this fashion elsewhere for the study of helical swimming in Stokes flow,⁵³ and helical swimming inside a capillary tube.⁴²

IV. ANALYSIS OF THE SWIMMING SPEED

While solving the Stokes equations with a general helical boundary is daunting, nearly cylindrical bodies may be studied by an asymptotic consideration. We will consider helical bodies of cross-sectional profile $1 + \varepsilon f(\theta)$, with $|\varepsilon| \ll 1$ and $f(\theta) = O(1)$. If the profile is described by a single Fourier mode, $f(\theta) = \cos(N\theta)$, then the operation $\varepsilon \rightarrow -\varepsilon$ is equivalent to a phase shift in $f(\theta)$, and there is no change in the swimming speed. We can therefore expect the swimming speed to appear only in even powers of ε . For general $f(\theta)$, this argument does not hold; nevertheless, we will show in Sec. IV A that the swimming speed still enters as $O(\varepsilon^2)$. Note also that when the axial wavelength $2\pi/\nu$ is small we can expect a straightforward asymptotic consideration in small ε to break down, though we will remedy this problem by a calculation accurate to $O(\varepsilon^4)$ in Sec. IV B. We will also show that the fourth-order expansion may be used to pick out the optimal pitch angle for a given cross-sectional profile.

A. The swimming speed, accurate to $O(\varepsilon^2)$

Assuming that $|\varepsilon| \ll 1$, we express the fluid velocity and swimming speed by a regular perturbation expansion with the notation

$$\mathbf{u}(r, \theta, \zeta) = \mathbf{u}_0(r, \theta, \zeta) + \varepsilon \mathbf{u}_1(r, \theta, \zeta) + \varepsilon^2 \mathbf{u}_2(r, \theta, \zeta) + O(\varepsilon^3), \quad (23)$$

$$U = U_0 + \varepsilon U_1 + \varepsilon^2 U_2 + O(\varepsilon^3). \quad (24)$$

Recall that in the frame moving with the helical geometry that the ζ dependence only appears in the varying basis vectors (see (11)); for example, we will write $\mathbf{u}_1(r, \theta, \zeta) = u_1(r, \theta)\hat{\mathbf{r}} + v_1(r, \theta)\hat{\boldsymbol{\theta}} + w_1(r, \theta)\hat{\boldsymbol{\zeta}}$. The leading order representation of the helical body is a rotating helical cylinder of unit radius. Expanding Eqs. (16) and (17) about small ε , the boundary conditions at leading order are given by

$$u_0(r = 1, \theta) = 0, \quad v_0(r = 1, \theta) = 1, \quad w_0(r = 1, \theta) = \frac{1}{\nu}, \quad (25)$$

$$u_0(r \rightarrow \infty, \theta) = v_0(r \rightarrow \infty, \theta) = 0, \quad w_0(r \rightarrow \infty, \theta) = \frac{1}{\nu} - U_0. \quad (26)$$

Since the domain is axisymmetric at leading order the fluid velocity may be assumed to be independent of θ , resulting in the leading order solutions to the Stokes equations, Eqs. (12)–(15), of

$$u_0 = 0, \quad v_0 = \frac{1}{r}, \quad w_0 = \frac{1}{v}, \quad p_0 = p_\infty. \quad (27)$$

The boundary conditions then show that $U_0 = 0$, as expected by the up-down symmetry of the cylinder.

We now proceed to determine the first order correction to the velocity field and swimming speed. The boundary conditions at the next order in the Taylor expansion of Eqs. (16) and (17) are

$$u_1(1, \theta) = 0, \quad v_1(1, \theta) = f(\theta) - f(\theta) \frac{\partial v_0}{\partial r} = 2f(\theta), \quad w_1(1, \theta) = 0, \quad (28)$$

$$u_1(\infty, \theta) = v_1(\infty, \theta) = 0, \quad w_1(\infty, \theta) = -U_1. \quad (29)$$

Adopting a Fourier expansion of the cross-sectional profile, we write

$$f(\theta) = \sum_{k=-\infty}^{\infty} \hat{f}_k e^{ik\theta}, \quad (30)$$

where $\hat{f}_k^* = \hat{f}_{-k}$ (the asterisk indicating complex conjugate), and $\hat{f}_0 = 0$ is assumed without loss of generality. Correspondingly, the pressure and fluid velocity are expressed in the Fourier basis as

$$p_1 = \sum_k \hat{p}_{1k} e^{ik\theta}, \quad \mathbf{u}_1 = \sum_k (\hat{u}_{1k} \hat{\mathbf{r}} + \hat{v}_{1k} \hat{\boldsymbol{\theta}} + \hat{w}_{1k} \hat{\mathbf{z}}) e^{ik\theta}, \quad (31)$$

with the summation over all integer values of k .

Matching terms of $O(\varepsilon)$ in the Stokes equations, Eqs. (12)–(15), we find that the modes are decoupled at this order as a consequence of linearity and homogeneity. Therefore, the Fourier coefficients for the velocity and pressure fields at first order must be linear in \hat{f}_k , and we may write

$$\hat{p}_{1k} = \mathcal{P}_k(r) \hat{f}_k, \quad \hat{u}_{1k} = \mathcal{U}_k(r) \hat{f}_k, \quad \hat{v}_{1k} = \mathcal{V}_k(r) \hat{f}_k, \quad \hat{w}_{1k} = \mathcal{W}_k(r) \hat{f}_k. \quad (32)$$

Since $\hat{f}_0 = 0$ by assumption, we have $\hat{u}_{10} = 0$ and $\hat{p}_{10} = 0$. For the remaining coefficients, as detailed in the Appendix B 1, we find expressions for the pressure and axial component of the fluid velocity,

$$\mathcal{P}_k = -ik D_k K_q(\lambda), \quad (33)$$

$$\mathcal{W}_k = \frac{D_k}{2v} \left(\lambda K_{q-1}(\lambda) - \frac{qv K_{q-1}(qv)}{K_q(qv)} K_q(\lambda) \right), \quad (34)$$

where $K_q(\cdot)$ is the q th modified Bessel function of the second kind, and we have defined $q = |k|$ and $\lambda = qvr$. The constants D_k are given by

$$D_k = \frac{4}{qK_q + qvK_{q-1} - \frac{2(q-2)K_{q-1}}{v} - \frac{(3q-2)K_{q-1}^2}{K_q} - \frac{qvK_{q-1}^3}{K_q^2}}, \quad (35)$$

where $K_{q-1} = K_{q-1}(qv)$ and $K_q = K_q(qv)$. Derivatives of velocity fields are easier to determine using Eqs. (12)–(15) at $r = 1$, and we find

$$\frac{d}{dr} \mathcal{U}_k \Big|_{r=1} = -2ik, \quad \frac{d}{dr} \mathcal{W}_k \Big|_{r=1} = J_q, \quad (36)$$

$$\frac{d}{dr} \mathcal{V}_k \Big|_{r=1} = vJ_q - qD_k(K_q(qv) + vK_{q-1}(qv)) - 2, \quad (37)$$

with

$$J_q = \frac{4q^2 K_{q-1} - 2q^2 \nu K_q + \frac{2q^2 \nu K_{q-1}^2}{K_q}}{q K_q + q \nu K_{q-1} - \frac{2(q-2)K_{q-1}}{\nu} - \frac{(3q-2)K_{q-1}^2}{K_q} - \frac{q \nu K_{q-1}^3}{K_q^2}}. \quad (38)$$

Since all modes describing the first order velocity field in the axial direction, w_1 , decay to 0 as $r \rightarrow \infty$ (in Eq. (34)), we find by inspection of the boundary conditions at infinity that $U_1 = 0$; hence, there is no first order correction to the swimming speed for any cross-sectional profile $f(\theta)$.

The calculation of the correction at $O(\varepsilon^2)$ is identical to the calculation at $O(\varepsilon)$, and it can be shown that the Fourier modes of the velocity field all vanish as $r \rightarrow \infty$ with the exception of the $k = 0$ mode. Focusing on the $k = 0$ mode, and using the same notation as in Eq. (31) at second order, we must have

$$\hat{u}_{20} = \frac{C_1}{r}, \quad \hat{v}_{20} = \frac{C_2}{r}, \quad \hat{w}_{20} = C_3, \quad \hat{p}_{20} = 0. \quad (39)$$

The constants are determined using the boundary conditions at second order,

$$u_2(1, \theta) = -f(\theta) \frac{\partial u_1(1, \theta)}{\partial r} = -f(\theta) \sum_k \hat{f}_k e^{ik\theta} \frac{d}{dr} \mathcal{U}_k \Big|_{r=1}, \quad u_2(\infty, \theta) = 0, \quad (40)$$

$$v_2(1, \theta) = -f(\theta) \frac{\partial v_1(1, \theta)}{\partial r} - f^2(\theta) = -f(\theta) \sum_k \hat{f}_k e^{ik\theta} \frac{d}{dr} \mathcal{V}_k \Big|_{r=1} - f^2(\theta), \quad v_2(\infty, \theta) = 0, \quad (41)$$

$$w_2(1, \theta) = -f(\theta) \frac{\partial w_1(1, \theta)}{\partial r} = -f(\theta) \sum_k \hat{f}_k e^{ik\theta} \frac{d}{dr} \mathcal{W}_k \Big|_{r=1}, \quad w_2(\infty, \theta) = -U_2. \quad (42)$$

Namely, we find

$$C_1 = \sum_k (-2ik) |\hat{f}_k|^2 = 0, \quad C_2 = - \sum_k |\hat{f}_k|^2 \frac{d}{dr} \mathcal{V}_k(1) - \sum_k |\hat{f}_k|^2, \quad C_3 = - \sum_k |\hat{f}_k|^2 J_q. \quad (43)$$

The swimming speed at $O(\varepsilon^2)$ is therefore given by a linear superposition of the solutions for each Fourier mode describing the profile $f(\theta)$,

$$U_2 = -\hat{w}_{20} = 2 \sum_{q \geq 1} J_q |\hat{f}_q|^2. \quad (44)$$

Figure 3(a) shows the normalized swimming speed of a rotating helical body described by a single Fourier mode, $f(\theta) = \cos(2\theta)$, for four values of ε , and for a wide range of helical pitches. The values computed using the full numerical simulations described in Sec. III are shown as symbols, while the theoretical prediction of Eq. (44) is shown as a solid line. The analytical prediction agrees well with the numerical results for small ν (large helical pitch) and as expected is more accurate for smaller ε . For larger values of ε , the analytical prediction begins to deteriorate at smaller values of ν . Intriguingly, the numerical simulations suggest an optimal choice of the pitch, $2\pi/\nu$, for a given amplitude, ε , but the non-monotonicity of the swimming speed is not captured in the $O(\varepsilon^2)$ theory.

The swimming speeds of helical bodies with cross-sectional profiles $f(\theta) = \cos(N\theta)$ are shown in Fig. 3(b) for four values of N , now fixing $\varepsilon = 0.1$, again for a wide range of pitches. The $O(\varepsilon^2)$ theory is shown by a solid line for each mode N , and we observe a monotonic and approximately linear increase in the predicted swimming speed as a function of N . It is clear that higher order terms must be taken into consideration for $N \geq 2$ to give satisfactory expressions of swimming speeds for bodies of all but the largest helical pitches.

Finally, recall that by subtracting the swimming speed from the fluid velocity, we find a solution to the problem of pumping by a rotating helical body with zero swimming speed. The rate of fluid transport as $r \rightarrow \infty$ in that case is precisely $-U\hat{z}$, with the speed U given by Eq. (44).

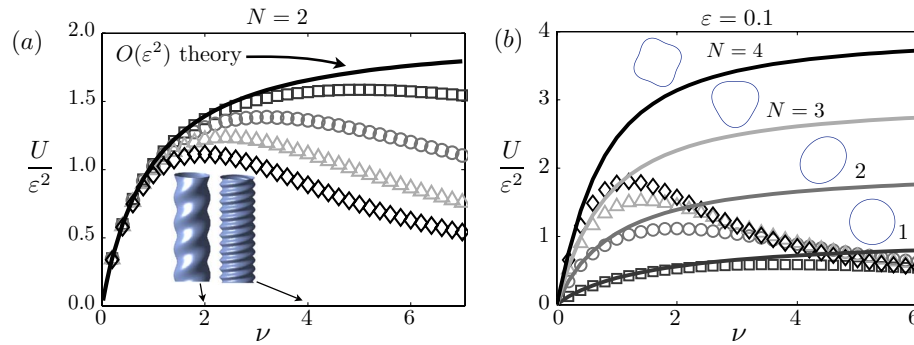


FIG. 3. (a) The normalized swimming speeds as functions of ν (the dimensionless helical pitch is given by $2\pi/\nu$) for wavenumber $N = 2$. Symbols indicate numerically computed swimming speeds with $\varepsilon = 0.025$ (squares), $\varepsilon = 0.05$ (circles), $\varepsilon = 0.075$ (triangles), and $\varepsilon = 0.1$ (diamonds). The solid line shows the prediction of the asymptotic theory from Eq. (44). Inset images are of helical bodies with $N = 2$ and $\varepsilon = 0.1$ with $\nu \in \{2, 4\}$. (b) The normalized swimming speeds for cross-sectional profiles $f(\theta) = \cos(N\theta)$, with $\varepsilon = 0.1$, as functions of ν . Again, symbols indicate numerically computed values, and solid curves indicate the $O(\varepsilon^2)$ theoretical predictions. Cross-sections of each surface are also shown.

Before proceeding to higher order terms, we pause for an entertaining calculation using the $O(\varepsilon^2)$ theory made possible by the decoupling of Fourier modes. Though it cannot be described by the current mathematical framework, consider a right-handed helical body onto which a left-handed helical pattern is grafted, as shown in Fig. 2(d). The structure is reminiscent of the double-wave structure of insect spermatozoa in the opposite chirality case⁵⁴ (see also Ref. 55). Upon rotation of such a body there will appear to be two waves passing along the surface moving in opposite directions. Using Eq. (44), the force-free translation of such a body can be predicted by subtracting the speeds corresponding to each cross-sectional description, and the swimming speed may vanish for suitably chosen parameters. The example shown in Fig. 2(d) is a right-handed helical body with surface deformation $\varepsilon_1 f(\theta) = 0.15 \cos(\theta)$ and $\nu = 1$ with a small left-handed helical perturbation of higher wavenumber, $\varepsilon_2 \tilde{f}(\theta) = 0.062 \cos(3\theta)$ and $\tilde{\nu} = 2$. Since the swimming speed increases rapidly with increasing wavenumber, a small amplitude perturbation ε_2 of high wavenumber may counteract the swimming of a low wavenumber shape of larger amplitude, ε_1 . The second order theory predicts a zero swimming speed for this example. More generally, writing the higher wavenumber perturbation in the form $\varepsilon_2 \tilde{f}(\theta)$, the resulting swimming speed (by superposition) is given by

$$U \approx \frac{\varepsilon_1^2}{2} J_1(\nu) - 2\varepsilon_2^2 \sum_{q \geq 1} |\tilde{f}_q|^2 J_q(\tilde{\nu}), \quad (45)$$

with J_q defined in Eq. (38), so that the swimming speed is predicted to vanish in the $O(\varepsilon^2)$ theory when

$$\varepsilon_2 = \frac{\varepsilon_1}{2} \sqrt{\frac{J_1(\nu)}{\sum_{q \geq 1} |\tilde{f}_q|^2 J_q(\tilde{\nu})}}. \quad (46)$$

B. The swimming speed, accurate to $O(\varepsilon^4)$

Already we have observed that the force-free swimming speed of a helical body exhibits a maximum value in the varying helical pitch, a feature of the dynamics not captured in the $O(\varepsilon^2)$ theory. Even in the simpler setting of a two-dimensional swimming Taylor sheet, remarkable non-monotonicity has been observed numerically and predicted in high-order asymptotic calculations.⁵⁶ We are therefore led to consider the next order correction to the swimming speed which will enter at $O(\varepsilon^4)$. As we approach the higher order correction to the swimming speed, note that many derivatives in θ are accompanied by a factor of ν as a consequence of Eq. (10). Balancing terms in Eq. (15), we should expect that $\partial u / \partial r = O(\nu)$, so that $\varepsilon^m \partial^m u / \partial r^m = O(\varepsilon^m \nu^m)$, which may be significant if ν is large. In this case we would find a boundary layer of thickness $O(\nu^{-1})$.

The correction to the swimming speed may be determined using the method of matched asymptotic expansions. In this approach, with ν assumed to be large, an inner variable $\xi = \nu(r - 1)$ is defined to magnify the dynamics near the body boundary. The solution in the inner variable, in the limit as $\xi \rightarrow \infty$, must match the limiting solution in the outer variable, r , as $r \rightarrow 1$ (see Ref. 57). In the problem of present interest, the outer solution is found by solving the Stokes equations order by order in a regular asymptotic expansion in ν^{-1} . Equations (12)–(15) show that the leading order equations in the outer problem are given by $\nu^2 \partial^2 u_0 / \partial \theta^2 = \nu^2 \partial^2 v_0 / \partial \theta^2 = \nu^2 \partial^2 w_0 / \partial \theta^2 = 0$, and hence the velocity field at leading order depends only on r . Studying the equations at the next order, we find that p_0, w_0 are constants, $u_0, v_0 \propto 1/r$, and that the velocity field at the subsequent order also depends only on r . Repeating the same argument, we see that the outer solution only contains the $k = 0$ mode, where the axial velocity w is a constant, equal to $1/\nu - U$ by the boundary condition at infinity. The $k \neq 0$ components of the flow are clearly nonzero near the body surface, but the above indicates that these modes must decay rapidly so as to allow for a match with the outer solution. Moreover, a match to the outer solution requires that the axial component of the velocity field in the inner problem limits to the constant $1/\nu - U$.

To solve the inner problem, the parameter $\delta = \varepsilon \nu$ is introduced. The variables are now expanded as a double series in both δ and ν^{-1} (see also Ref. 58). The $O(\varepsilon^2)$ theory is expected to be accurate only when $\delta \ll 1$. Higher order corrections are therefore required when $\delta = O(1)$, which we now perform for cross-sectional profiles described by a single Fourier mode, $f(\theta) = \cos(N\theta)$. Instead of computing the full $O(\delta^4)$ solution, we will instead compute only the first several significant terms in the expansion (to be specific, the $\delta^4 \nu^{-2}$ and $\delta^4 \nu^{-1}$ terms).

We begin by defining

$$S_1(\nu, \xi) = \sum_{n \geq 0} (-1)^n \nu^{-(n+1)} \xi^n, \quad (47)$$

$$S_2(\nu, \xi) = \sum_{n \geq 0} (-1)^n (n+1) \nu^{-n-2} \xi^n. \quad (48)$$

The Stokes equations may then be written as

$$p_{\xi\xi} + S_1(\nu, \xi) p_{\xi} + (1 + S_2(\nu, \xi)) p_{\theta\theta} = 0, \quad (49)$$

$$u_{\xi\xi} + 3S_1(\nu, \xi) u_{\xi} + S_2(\nu, \xi) u + (1 + S_2(\nu, \xi)) u_{\theta\theta} = \frac{1}{\nu} p_{\xi} + 2S_1(\nu, \xi) w_{\theta}, \quad (50)$$

$$w_{\xi\xi} + S_1(\nu, \xi) w_{\xi} + (1 + S_2(\nu, \xi)) w_{\theta\theta} = -\frac{1}{\nu} p_{\theta}, \quad (51)$$

$$u_{\xi} + S_1(\nu, \xi)(u + v_{\theta}) - w_{\theta} = 0. \quad (52)$$

A similar equation for v may be derived but is not required for this calculation. The no-slip boundary condition is similarly described,

$$\mathbf{u}(\xi = \delta f(\theta), \theta) = (1 + \delta \nu^{-1} f(\theta)) \hat{\boldsymbol{\theta}} + \frac{1}{\nu} \hat{\mathbf{z}}. \quad (53)$$

Upon expanding in a Taylor series the order-by-order boundary conditions are found,

$$\sum_{m=0}^{+\infty} \frac{1}{m!} \delta^m f(\theta)^m \frac{\partial^m u}{\partial \xi^m} = 0, \quad \sum_{m=0}^{+\infty} \frac{1}{m!} \delta^m f(\theta)^m \frac{\partial^m v}{\partial \xi^m} = 1 + \delta \nu^{-1} f(\theta), \quad (54)$$

$$\sum_{m=0}^{+\infty} \frac{1}{m!} \delta^m f(\theta)^m \frac{\partial^m w}{\partial \xi^m} = \nu^{-1}. \quad (55)$$

The $m = 0$ and $m = 1$ solutions have already appeared in Sec. IV A. However, while the $m = 0$ solution is easily expressed in terms of ν and ξ , this is not the case for the $m = 1$ solution, which we will require. Therefore, we now solve again for the $m = 1$ solution but using the new framework

above. According to the boundary conditions and the solution for $m = 0$, we are motivated to assume the following forms for the pressure, velocity, and swimming speed:

$$p = p_\infty + \sum_{m \geq 1} \delta^m v^{-1} \sum_{n=0}^{\infty} v^{-n} p_{mn}, \quad (56)$$

$$\mathbf{u} = \left(\sum_{n \geq 0} (-1)^n v^{-n} \xi^n \hat{\boldsymbol{\theta}} + v^{-1} \hat{\mathbf{z}} \right) + \sum_{m \geq 1} \delta^m v^{-1} \sum_{n=0}^{\infty} v^{-n} (u_{mn} \hat{\mathbf{r}} + v_{mn} \hat{\boldsymbol{\theta}} + w_{mn} \hat{\mathbf{z}}), \quad (57)$$

$$U = \sum_{m \geq 1} \delta^m v^{-1} \sum_{n=0}^{\infty} v^{-n} U_{mn}. \quad (58)$$

Noting that the coupling for different powers of m only appear in the boundary conditions, the $m = 1$ terms may be solved for every n before moving on to the $m = 2$ terms, and so on. Below, we will need only to solve for the axial fluid velocity, w , up to $n = 2$, or $O(v^{-3})$ for $m = 1, 2, 3$ to guarantee $O(\varepsilon^4)$ accuracy.

The details of the following calculation are included as Appendix B 2. To summarize, denoting the k th mode solution to $(\partial_{\xi\xi} + \partial_{\theta\theta})H = 0$ by

$$H_k(\xi, \theta) = \exp(-q\xi)e^{ik\theta}, \quad (59)$$

with $q = |k|$, the $m = 1$ asymptotic solutions for a general boundary profile $f(\theta) = \sum_k \hat{f}_k e^{ik\theta}$ are given by

$$p_{m=1} = -v^{-1} \sum_{k \neq 0} 4ik \hat{f}_k H_k + v^{-2} \sum_{k \neq 0} \hat{f}_k \left(2ik\xi + \frac{6ik}{q} \right) H_k + O(v^{-3}), \quad (60)$$

$$u_{m=1} = v^{-2} \sum_{k \neq 0} (-2ik \hat{f}_k) \xi H_k + v^{-3} \sum_{k \neq 0} ik \hat{f}_k \xi^2 H_k + O(v^{-4}), \quad (61)$$

$$v_{m=1} = v^{-1} \sum_{k \neq 0} 2 \hat{f}_k H_k - v^{-2} \sum_{k \neq 0} \hat{f}_k \xi H_k + O(v^{-3}), \quad (62)$$

$$w_{m=1} = v^{-2} \sum_{k \neq 0} 2q \hat{f}_k \xi H_k - v^{-3} \sum_{k \neq 0} (3\xi + q\xi^2) \hat{f}_k H_k + O(v^{-4}), \quad (63)$$

where $H_k = H_k(\xi, \theta)$. For $m \geq 2$, we consider only helical shapes with $f(\theta) = \cos(N\theta)$, or $\hat{f}_N = \hat{f}_{-N} = 1/2$ and $\hat{f}_k = 0$ for $|k| \neq N$. By a similar calculation as for the solutions at $m = 1$, the solutions at $m = 2$ are given by

$$p_{m=2} = 2\Re \left[-v^{-1} 2iN^2 H_{2N} + v^{-2} (iN^2 \xi + 4iN) H_{2N} \right] + O(v^{-3}), \quad (64)$$

$$u_{m=2} = 2\Re \left[v^{-2} \left(-iN^2 \xi + \frac{iN}{2} \right) H_{2N} + v^{-3} \left(iN \xi + \frac{iN^2}{2} \xi^2 \right) H_{2N} \right] + O(v^{-4}), \quad (65)$$

$$v_{m=2} = v^{-1} N - v^{-2} N \xi + 2\Re \left[v^{-1} \frac{N}{2} H_{2N} - v^{-2} \frac{3N}{4} \xi H_{2N} \right] + O(v^{-3}), \quad (66)$$

$$w_{m=2} = -Nv^{-2} + \frac{3}{2}v^{-3} + 2\Re \left[v^{-2} \left(N^2 \xi - \frac{N}{2} \right) H_{2N} + v^{-3} \frac{3 - 7N\xi - 2N^2 \xi^2}{4} H_{2N} \right] + O(v^{-4}), \quad (67)$$

where $\Re[\cdot]$ denotes the real part of the argument. By investigation of the boundary condition for $w_{m=4}$, only the N th mode of w in the $m = 3$ solution is needed to compute the fourth-order swimming

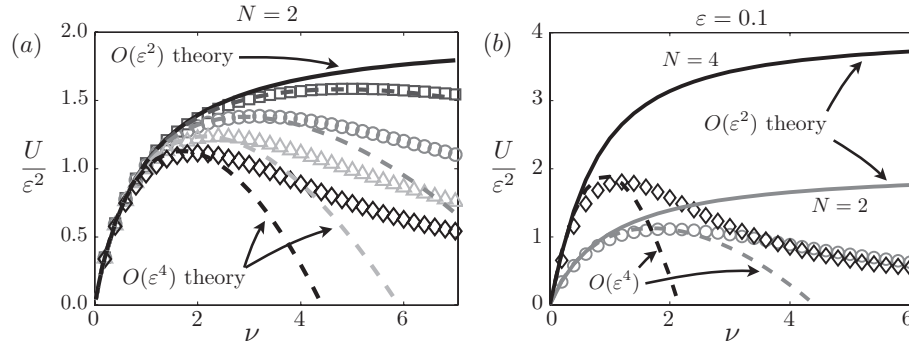


FIG. 4. (a) As in Fig. 3, the normalized swimming speeds for $N = 2$ fixed are shown as functions of ν for a selection of ε . Symbols indicate numerically computed swimming speeds with $\varepsilon = 0.025$ (squares), $\varepsilon = 0.05$ (circles), $\varepsilon = 0.075$ (triangles), and $\varepsilon = 0.1$ (diamonds). The solid line shows the $O(\varepsilon^2)$ result from Eq. (44), while the dashed lines show the $O(\varepsilon^4)$ predictions. (b) Normalized swimming speeds are shown for bodies with $f(\theta) = \cos(N\theta)$ for two Fourier modes, $N = 2$ and $N = 4$, with $\varepsilon = 0.1$ fixed.

speed, $U_{m=4}$. By a similar calculation it can be shown that

$$w_{m=3} = 2\Re \left[-\nu^{-2} \frac{3N^2\xi + 2N^2}{8} H_N + \nu^{-3} \frac{14N + N^2\xi + 3N^3\xi^2}{16} H_N + (\dots) H_{3N} \right] + O(\nu^{-4}). \quad (68)$$

Only the zeroth Fourier mode of $w_{m=4}$ is required to determine the swimming speed. Noting that

$$w_{m=4,k=0} = -\frac{1}{2\pi} \int_0^{2\pi} \left\{ f(\theta) \partial_\xi w_{m=3} + \frac{1}{2} f^2(\theta) \partial_\xi^2 w_{m=2} + \frac{1}{6} f^3(\theta) \partial_\xi^3 w_{m=1} \right\} d\theta, \quad (69)$$

we finally arrive at the fourth-order correction to the swimming speed for finite ν ,

$$U_{m=4} = -\nu^{-2} \frac{5N^3}{4} + \nu^{-3} \frac{3N^2}{2} + O(\nu^{-4}). \quad (70)$$

Therefore, a rotating helical body of cross-sectional profile $\rho(\theta) = 1 + \varepsilon \cos(N\theta)$ swims with zero net force at the speed

$$U = \varepsilon^2 \left(\frac{1}{2} J_N - \varepsilon^2 \nu^2 \frac{5N^3}{4} + \varepsilon^2 \nu \frac{3N^2}{2} \right) + O(\varepsilon^4) + O(\varepsilon^6 \nu^4), \quad (71)$$

with J_N given in (38).

We can now revisit the comparison between the analytical predictions and the results of the full numerical simulations. Figure 4(a) shows the swimming speeds for the same cases considered in Fig. 3(a), but here we include as dashed lines the predictions of the $O(\varepsilon^4)$ theory from Eq. (71). The $O(\varepsilon^4)$ theory shows a significant improvement in the prediction for larger values of both ε and ν . In particular, the speed-maximizing value of ν , and the maximum swimming speed, are very well approximated for the values of ε considered. This optimal value of ν will be discussed in Sec. V. Similarly, Fig. 4(b) reproduces the results from Fig. 3(b), but now includes the $O(\varepsilon^4)$ predictions for two different Fourier modes, $N = 2$ and $N = 4$.

C. Computing the torque to $O(\varepsilon^2)$

The external torque required to rotate the helical body may be computed using the solutions already derived above, which we provide up to $O(\varepsilon^2)$. The torque per unit length is given by integration of the fluid stress,

$$L = -\hat{\mathbf{z}} \cdot \int_0^{2\pi} \mathbf{y} \times [\boldsymbol{\sigma} \cdot (\mathbf{y}_\theta \times \mathbf{y}_\zeta)] \Big|_{\zeta=0} d\theta = - \int_0^{2\pi} (\rho^2 \sigma_{\theta r} - \rho \rho_\theta \sigma_{\theta\theta} + \nu \rho^2 \rho_\theta \sigma_{\theta z}) d\theta, \quad (72)$$

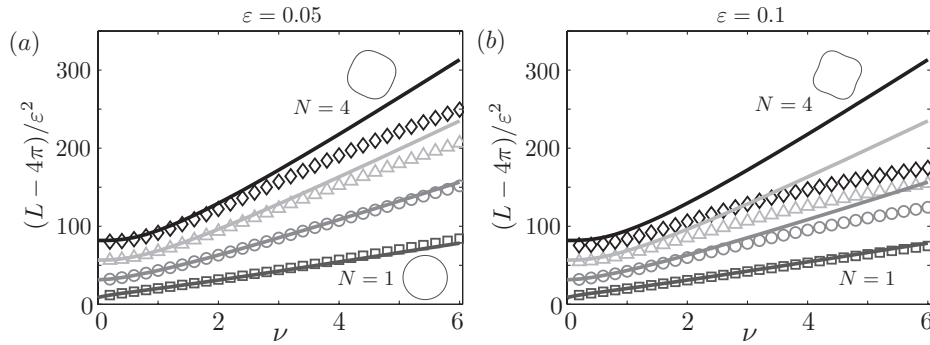


FIG. 5. The normalized torque per unit length as a function of ν for four wavenumbers, N , with: (a) $\varepsilon = 0.05$ fixed and (b) $\varepsilon = 0.1$ fixed. Symbols indicate numerically computed values, and solid lines show the asymptotic predictions from Eq. (74).

where $\rho(\theta) = 1 + \varepsilon f(\theta)$. The required velocities are found by expanding about $\rho = 1$, keeping terms up to $O(\varepsilon^2)$. Inserting velocity and pressure fields, we arrive at

$$L = 4\pi + 2\pi\varepsilon^2 \left(\hat{v}_{20} - \frac{d\hat{v}_{20}}{dr} \right) \Big|_{r=1} - \varepsilon^2 \int_0^{2\pi} \left\{ f'(\theta) p_1 + \left(-v_1 + \frac{\partial v_1}{\partial r} + \frac{\partial^2 v_1}{\partial r^2} \right) f(\theta) + f(\theta) \frac{\partial u_1}{\partial \theta} + f(\theta) \frac{\partial^2 u_1}{\partial r \partial \theta} - 2f'(\theta) u_1 + \nu f'(\theta) \frac{\partial w_1}{\partial \theta} - (2 + \nu^2) f'(\theta) \frac{\partial v_1}{\partial \theta} \right\} \Big|_{r=1} d\theta. \quad (73)$$

The integral is zero by the Stokes equations and incompressibility in $O(\varepsilon)$ order, which results in the torque per unit length on the body,

$$L = 4\pi + 4\pi\varepsilon^2 \sum_{q \geq 1} |f_q|^2 \left(2q D_q [K_q(q\nu) + \nu K_{q-1}(q\nu)] - 2\nu J_q + 2 \right), \quad (74)$$

with D_q , J_q , K_q , and K_{q-1} as defined in Sec. IV A.

The approximations for the torque per unit length are plotted as solid lines in Figs. 5(a) and 5(b) for the first four Fourier modes describing $f(\theta)$. The torques computed using the full numerical solutions of the Stokes equations are included as symbols. The nearly linear increase in the torque per unit length as a function of N is primarily due to the linear scaling of the body wavelength in the axial (\hat{z}) direction with N . The asymptotic approximation is naturally improved for small ε , small N , and small ν . The curves correspond to the cases shown in Fig. 3(b).

V. OPTIMAL HELICAL GEOMETRIES

For some applications in biological or engineering design, it may be desirable to select a helical body or drill geometry from a prescribed class \mathcal{C} to maximize the swimming or pumping speed. In other situations, the optimal helical surface might be that in \mathcal{C} which provides a given translational speed for minimal torque. In the small perturbation regime of present interest, the dimensionless torque is approximately 4π for all bodies, which is the torque required to rotate the base cylindrical shape. We would like to determine a surface topography that maximizes the dimensionless swimming speed U for a fixed rotation rate. We have already seen, for instance, in Fig. 4, that there exists a value of ν which maximizes the swimming speed for a given surface pattern. To further simplify the problem, we consider the class \mathcal{C}_ε of helical bodies described by a single Fourier mode, $f(\theta) = \cos(N\theta)$, with ε fixed; \mathcal{C}_ε is then parametrized by N and ν .

A clear feature shown in Fig. 3 is that the swimming speed initially increases with ν to a maximum value and then decreases in every case considered. Using the estimated swimming speed from Eq. (71), an optimal choice of ν may be approximated for a given mode N . For reasonably

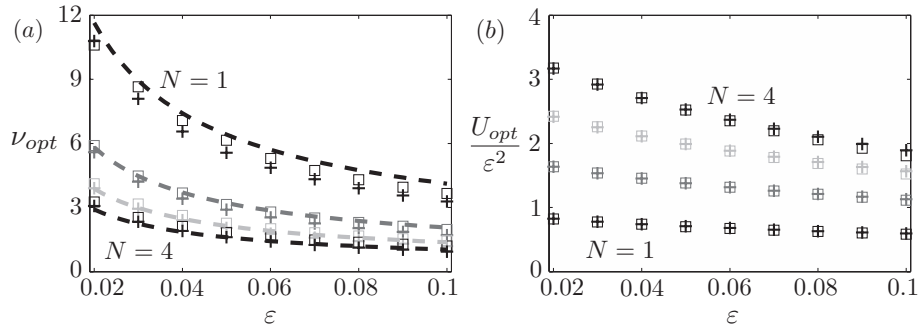


FIG. 6. (a) The plots for v_{opt} for different ϵ values. Lines are predictions by Eq. (76); plus signs are the maximum points of Eq. (71) found by a binary search; squares are plots for the numerical results. (b) The swimming speeds at the optimal helical pitch, setting $v = v_{opt}$.

small N and $O(1) < v < 1/\epsilon$, Eq. (71) has the following asymptotic form:

$$\frac{U}{\epsilon^2} \approx N - \frac{3}{2v} + \epsilon^2 N^2 v \left(\frac{3}{2} - \frac{5Nv}{4} \right), \quad (75)$$

from which the optimal value of v , denoted by v_{opt} , is found to be

$$v_{opt} \approx \frac{1}{N} \left(\frac{3}{5\epsilon^2} \right)^{1/3}. \quad (76)$$

Recall that the parameter $\delta = \epsilon v$ must be small for the double series expansion to return an accurate approximation of the swimming speed. Equation (76) is expected to be accurate if $\epsilon v_{opt} \approx \epsilon^{1/3} \ll 1$; for instance, to have $\epsilon^{1/3} \lesssim 0.5$ we require $\epsilon \lesssim 0.12$.

Figures 6(a) and 6(b) show the values of v_{opt} and the corresponding swimming speed, U_{opt} , as functions of ϵ , as determined numerically using the full simulations (squares), by maximizing Eq. (71) numerically (plus signs), and from the approximation (76) (dashed lines). Although there is a systematic error in the theoretical prediction of v_{opt} , the agreement indicates the success of the theory in this regime.

We now consider the effect of varying N for fixed v . Although they are not equivalent, doubling N at least has a similar effect on the observed helical geometry as doubling v . The approximation formula (75) is not accurate for large N , however, so based on the work above we do not have an accurate representation of the optimal mode N_{opt} . We are still free to compute the optimal value of N for given values of ϵ and v , and we show the results of this numerical investigation in Table I. The swimming speeds shown in the table are of the form U_N , where the speed-maximizing choice of wavenumber, $N = N_{opt}$, is determined numerically. We observe that in this regime the optimal mode N_{opt} decreases as v and ϵ increase.

To rationalize the observations of N_{opt} , note that Eq. (75), though inaccurate for large N , is of the form $U = Ng(Nv)$. If this trend were to continue with the calculation of yet higher order terms in the expansion (i.e., if the representation of U is still written as $U = Ng(Nv)$ for a more complicated function $g(Nv)$), then we will find $N_{opt} \sim C(\epsilon)/v$, which is roughly what we observe in the numerical investigation as reported in Table I.

TABLE I. Optimal swimming speed, choosing the computed value $N = N_{opt}$, for fixed v .

v	$\epsilon = 0.05$	$\epsilon = 0.075$	$\epsilon = 0.1$
1	$U_{14}/\epsilon^2 = 4.37$	$U_9/\epsilon^2 = 2.87$	$U_7/\epsilon^2 = 2.12$
2	$U_9/\epsilon^2 = 3.37$	$U_6/\epsilon^2 = 2.18$	$U_5/\epsilon^2 = 1.59$
3	$U_6/\epsilon^2 = 2.51$	$U_4/\epsilon^2 = 1.61$	$U_3/\epsilon^2 = 1.17$

We have also investigated the question of the optimal helical geometry which maximizes the swimming speed for a given torque. Since the swimming speed and the torque both depend linearly upon the rotation rate, this issue is addressed by maximizing the ratio U/L , where U is the swimming speed plotted in Fig. 3, and L is the torque plotted in Fig. 5. However, since the computed torques shown in Fig. 5 vary only modestly with variations in the geometry in the regime of interest, we find very little variation in the geometry which maximizes U/L compared to the geometry which maximizes U . This may not be the case for the passage of helical waves in the nearly cylindrical regime, which unlike in the present consideration does not include the generation of a base rotational flow by the rotating cylindrical shape at leading order. Optimizing helical geometries in helical wave swimming and pumping is expected to depend more significantly upon the chosen efficiency metric.

VI. DISCUSSION

In this paper, we studied the force-free swimming or fluid pumping by helical bodies of arbitrary cross-section numerically, and analytically in the case of small-amplitude deviations from a cylindrical base shape. Helical symmetry was used to reduce the dimensionality of the system, making possible both the numerical and analytical efforts. The leading order swimming speed, which entered at $O(\varepsilon^2)$, was found to be a superposition of the Fourier components describing the cross-sectional geometry. By comparing the predictions to numerically determined values, the leading order result was found to be accurate for all bodies of sufficiently small helical pitch angle. A much more accurate prediction was then provided up to $O(\varepsilon^4)$ and for larger pitch angles for bodies with cross-sections described by a single Fourier mode. These results were used to rationalize the numerically determined optimal helical pitch for a given cross-sectional wavenumber N , or the optimal wavenumber for a given helical pitch. Solutions to the problem of pumping by a rotating helical body with zero swimming speed were simultaneously derived; the rate of fluid transport at infinity in the pumping problem is identical to the force-free swimming speed.

The results shown here may be useful for designing efficient synthetic microswimmers, for developing pumping mechanisms in microscale environments, and for drilling strategies for highly viscous fluids at macroscopic scales. For example, the rotation of a double-helical body with opposite chirality shown in Fig. 2(d) may produce useful mixing patterns in a fluid while placing minimal axial strain on the helical agitator. We can envision such a helically patterned nearly cylindrical surface for such use in microfluidic devices.^{59,60} In the future, we hope to explore in more detail the behavior of complex fluids, such as viscoelastic and anisotropic fluids, when driven by an immersed helical body.^{37,61} Filament flexibility and internal molecular motor dynamics may also play critical roles in many problems of biological interest, for which the theory presented here will provide either a test for numerical methods, or a launching point for analytical investigations.

The passage of helical waves, which differs from rigid body motion, can be studied using the same framework as described in this paper. In particular, by passing helical waves along a surface a body can swim or pump without need of an external torque. This will have considerable consequences for the computation of the mechanical work done on the fluid during swimming, which may result in an interesting investigation of optimal geometries in that case. The study of helical waves is important in the study of swimming by ciliated organisms such as *Paramecium* and *Volvox*,^{62,63} and even more directly in such organisms as the marine bacterium *Synechococcus* (see Refs. 64–68). Swimming and pumping by helical waves will be the topic of a subsequent paper.

APPENDIX A: VALIDATION OF THE NUMERICAL METHOD

The numerical method used in the paper is partially validated by comparison with the small-amplitude asymptotic solutions derived above. For helical shapes of more considerable geometric variation, we now perform a convergence study. Consider the helical shape described by the in-plane curve $\rho(\theta) = 1 + \varepsilon f(\theta) = 1 + (1/3)(\cos(\theta) - \sin(3\theta))$ and $\nu = 1$, as shown in Fig. 1. Table II shows

TABLE II. Three convergence studies: (1) varying M , with $N_W = 5$ and $N_A/N_W = 16$ fixed; (2) varying N_A , with $N_W = 5$ and $M = 16$ fixed; (3) varying N_W , with $N_A/N_W = 16$ and $M = 16$ fixed.

M	U	L	N_A/N_W	U	L	N_W	U	L
16	0.081733	19.60312	12	0.078402	19.59587	6	0.082795	19.59965
32	0.081090	19.57638	24	0.081149	19.61341	12	0.084734	19.58195
64	0.081018	19.57598	48	0.080930	19.60641	24	0.085422	19.57128
128	0.081019	19.57599	96	0.080938	19.60708	48	0.085432	19.56992

the results of increasing the number of azimuthal gridpoints, M , the number of axial gridpoints, N_A , and the number of wavelengths, N_W . Convergence in the azimuthal resolution and the axial resolution per wavelength (through N_A/N_W) are rapid, as expected from Gaussian quadrature, and convergence is also rapid with increasing numbers of wavelengths, N_W . Note that the highly resolved case $(M, N_A/N_W, N_W) = (32, 24, 24)$ gives $(U, L) = (0.085341, 19.54007)$. The results suggest that the true values are computed to within 1% using only $(M, N_A/N_W, N_W) = (16, 24, 12)$, which in this example gives $(U, L) = (0.084871, 19.57795)$.

APPENDIX B: DETAILS OF THE VELOCITY FIELD CALCULATIONS

1. Derivation of the Fourier coefficients in Sec. IV A

To compute the Fourier coefficients of the velocities for $k \neq 0$, we set $f(\theta) = \exp(ik\theta)$, and write $p_1 = \mathcal{P}_k \exp(ik\theta)$ and $\mathbf{u}_1 = u_1 \hat{\mathbf{r}} + v_1 \hat{\boldsymbol{\theta}} + w_1 \hat{\mathbf{z}} = (\mathcal{U}_k \hat{\mathbf{r}} + \mathcal{V}_k \hat{\boldsymbol{\theta}} + \mathcal{W}_k \hat{\mathbf{z}}) \exp(ik\theta)$. Matching terms of $O(\varepsilon)$ in the momentum balance equation, and taking the divergence, we have using incompressibility that $\Delta p_1 = 0$. Letting $\lambda = qvr$, this equation may be converted to the modified Bessel equation,

$$\left(\lambda^2 \frac{d^2}{d\lambda^2} + \lambda \frac{d}{d\lambda} - (\lambda^2 + q^2) \right) \mathcal{P}_k = 0, \quad (\text{B1})$$

which gives

$$\mathcal{P}_k = -ik D_k K_q(\lambda) = -ik D_k K_q(qvr), \quad (\text{B2})$$

where $K_q(\cdot)$ is the modified Bessel function of the second kind, $q = |k|$, and D_k are unknown, real constants. Inserting this expression into the equation for w_1 (the $O(\varepsilon)$ terms in Eq. (14)) results in

$$\left(\lambda^2 \frac{d^2}{d\lambda^2} + \lambda \frac{d}{d\lambda} - (\lambda^2 + q^2) \right) \mathcal{W}_k = -\frac{D_k}{v} \lambda^2 K_q(\lambda). \quad (\text{B3})$$

With the boundary condition $\mathcal{W}_k|_{r=1} = 0$, we find

$$\mathcal{W}_k = \frac{D_k}{2v} \left(\lambda K_{q-1}(\lambda) - \frac{qv K_{q-1}(qv)}{K_q(qv)} K_q(\lambda) \right). \quad (\text{B4})$$

Meanwhile, in the equation for u_1 (the $O(\varepsilon)$ terms in Eq. (12)), the incompressibility condition is used to remove the $\partial_\theta v$ term, and we obtain

$$\frac{\partial^2 u_1}{\partial r^2} + \frac{3}{r} \frac{\partial u_1}{\partial r} + \frac{u_1}{r^2} + \frac{1}{r^2} \frac{\partial^2 u_1}{\partial \theta^2} + v^2 \frac{\partial^2 u_1}{\partial \theta^2} = \frac{2v}{r} \frac{\partial w_1}{\partial \theta} + \frac{\partial p_1}{\partial r}. \quad (\text{B5})$$

Writing $u_1 = \mathcal{U}_k \exp(ik\theta)$, we have

$$\left(\lambda^2 \frac{d^2}{d\lambda^2} + \lambda \frac{d}{d\lambda} - (q^2 + \lambda^2) \right) (\lambda \mathcal{U}_k) = \lambda (-ik D_k \frac{\lambda^2}{qv} K'_q(\lambda) + 2i \text{sign}(k) \lambda \mathcal{W}_k), \quad (\text{B6})$$

which is solved to give

$$\mathcal{U}_k = ik E_k \frac{K_q(\lambda)}{\lambda} - \frac{ik D_k}{qv} \left(\frac{1}{2} \lambda K_q(\lambda) - \frac{1}{2} \left(q - 2 + \frac{qv K_{q-1}(qv)}{K_q(qv)} \right) K_{q-1}(\lambda) \right), \quad (\text{B7})$$

where E_k are additional unknown constants. Using the boundary condition $\mathcal{U}_k|_{r=1} = 0$ and the incompressibility condition, we find

$$\mathcal{U}_k \Big|_{\lambda=qv} = 0, \quad \frac{d}{d\lambda} \mathcal{U}_k \Big|_{\lambda=qv} = -\frac{2ik}{qv}, \quad (\text{B8})$$

where $q = |k|$. These two conditions may be used to solve for the constants E_k and D_k ; the latter are provided in (35), which entirely describe \mathcal{P}_k and \mathcal{W}_k , which are then used in the calculation of the swimming speed in the paper.

2. Details for deriving the asymptotic solution in Sec. IV B

We now provide details for the calculation of the $m = 1$ solution in Sec. IV B. As we will restrict our attention to the $m = 1$ solution here, for clarity we omit the index for m and keep only the index for n . For example, u should be interpreted as $u_{m=1}$ and u_0 should be interpreted as u_{10} .

Working in the inner variable $\xi = v(r - 1)$, the boundary condition on the velocity field at first order is given by

$$u(\xi = 0, \theta) = 0, \quad v(\xi = 0, \theta) = \frac{2}{v} f(\theta), \quad w(\xi = 0, \theta) = 0. \quad (\text{B9})$$

The incompressibility condition may be used to find the last boundary condition needed in the following calculation:

$$u_\xi(\xi = 0, \theta) = -\frac{1}{v} v_\theta = -\frac{2}{v^2} f'(\theta). \quad (\text{B10})$$

The equation for p_0 is $\partial_{\xi\xi} p_0 + \partial_{\theta\theta} p_0 = 0$, which has the solution

$$p_0 = \sum_{k \neq 0} A_k \exp(-q\xi) \exp(ik\theta), \quad (\text{B11})$$

with $q = |k|$ and A_k as yet to be determined constants. Since only the gradient of the pressure appears in the Stokes equations, the $k = 0$ mode of the pressure may be chosen to be 0 without loss of generality. At the next order, we find $\partial_{\xi\xi} p_1 + \partial_{\theta\theta} p_1 = -\partial_\xi p_0$, which has the solution

$$p_1 = \sum_{k \neq 0} -\frac{A_k}{2} \xi \exp(-q\xi) \exp(ik\theta) + \sum_{k \neq 0} A_{1k} \exp(-q\xi) \exp(ik\theta), \quad (\text{B12})$$

introducing new unknown constants A_{1k} .

Meanwhile, the equation for w_0 is $\partial_{\xi\xi} w_0 + \partial_{\theta\theta} w_0 = 0$, so that $w_0 = 0$. We recall that the next order equation is $\partial_{\xi\xi} w_1 + \partial_{\theta\theta} w_1 = -\partial_\theta p_0$, and solving, we find

$$w_1 = \sum_{k \neq 0} \frac{ikA_k}{2q} \xi \exp(-q\xi) \exp(ik\theta). \quad (\text{B13})$$

Then, to determine the constants A_k , we move on to consider the radial part of the velocity field, u . By a similar calculation we find $u_0 = 0$, and from $\partial_{\xi\xi} u_1 + \partial_{\theta\theta} u_1 = \partial_\xi p_0$, we find

$$u_1 = \sum_{k \neq 0} \frac{A_k}{2} \xi \exp(-q\xi) \exp(ik\theta). \quad (\text{B14})$$

Applying the boundary conditions, the constants are given by

$$A_k = -4ik \hat{f}_k. \quad (\text{B15})$$

Finally, matching terms in the incompressibility condition results in the relation $\partial_\theta v_0 = \partial_\theta w_1 - \partial_\xi u_1 - u_0$, yielding

$$v_0 = \sum_{k \neq 0} 2\hat{f}_k \exp(-q\xi) \exp(ik\theta). \quad (\text{B16})$$

We now have our disposal the fields p_0 , u_1 , w_1 , and v_0 . Moving on to the second order calculation, we come to the equation for u_2 , $\partial_{\xi\xi}u_2 + \partial_{\theta\theta}u_2 = \partial_{\xi}p_1 + 2\partial_{\theta}w_1 - 3\partial_{\xi}u_1$. Solving,

$$u_2 = \sum_{k \neq 0} \left(\frac{A_k}{q} + \frac{1}{2}A_{1k} - \frac{A_k}{4q} \right) \xi \exp(-q\xi) \exp(ik\theta) - \sum_{k \neq 0} \frac{A_k}{4} \xi^2 \exp(-q\xi) \exp(ik\theta). \quad (\text{B17})$$

Applying the boundary conditions, we then find

$$A_{1k} = -\frac{3A_k}{2q} = \frac{6ik}{q} \hat{f}_k, \quad (\text{B18})$$

$$u_2 = \sum_{k \neq 0} -\frac{A_k}{4} \xi^2 \exp(-q\xi) \exp(ik\theta). \quad (\text{B19})$$

Looking to the equation for w_2 , we have $\partial_{\xi\xi}w_2 + \partial_{\theta\theta}w_2 = -\partial_{\theta}p_1 - \partial_{\xi}w_1$, resulting in the solution

$$w_2 = \sum_{k \neq 0} -\frac{ikA_k}{2q^2} \xi \exp(-q\xi) \exp(ik\theta) + \sum_{k \neq 0} -\frac{1}{4q} ikA_k \xi^2 \exp(-q\xi) \exp(ik\theta) \quad (\text{B20})$$

$$+ \sum_{k \neq 0} -\frac{1}{4q^2} ikA_k \xi \exp(-q\xi) \exp(ik\theta). \quad (\text{B21})$$

Finally, v_1 is found by solving $\partial_{\theta}v_1 = \partial_{\theta}w_2 - \partial_{\xi}u_2 - u_1 + \xi\partial_{\theta}v_0$.

- ¹ T. Koetsier and H. Blauwendraat, "The Archimedean screw-pump: A note on its invention and the development of the theory," in *Proceedings of the International Symposium on History of Machines and Mechanisms, 2004* (Springer, Netherlands, 2004), pp. 181–194.
- ² P. A. Tanguy, R. Lacroix, F. Bertrand, L. Choplin, and E. B. De La Fuente, "Finite element analysis of viscous mixing with a helical ribbon-screw impeller," *AIChE J.* **38**, 939–944 (1992).
- ³ J. De La Villeon, F. Bertrand, P. A. Tanguy, R. Labrie, J. Bousquet, and D. Lebouvier, "Numerical investigation of mixing efficiency of helical ribbons," *AIChE J.* **44**, 972–977 (1998).
- ⁴ G. Delaplace, J. C. Leuliet, and V. Relandeau, "Circulation and mixing times for helical ribbon impellers: Review and experiments," *Exp. Fluids* **28**(2), 170–182 (2000).
- ⁵ M. Robinson and P. W. Cleary, "Flow and mixing performance in helical ribbon mixers," *Chem. Eng. Sci.* **84**, 382–398 (2012).
- ⁶ P. J. Carreau, I. Patterson, and C. Y. Yap, "Mixing of viscoelastic fluids with helical-ribbon agitators. I. Mixing time and flow patterns," *Can. J. Chem. Eng.* **54**, 135–142 (1976).
- ⁷ F. Jiang, K. S. Drese, S. Hardt, M. Küpper, and F. Schönfeld, "Helical flows and chaotic mixing in curved micro channels," *AIChE J.* **50**, 2297–2305 (2004).
- ⁸ T. Honda, K. I. Arai, and K. Ishiyama, "Micro swimming mechanisms propelled by external magnetic fields," *IEEE Trans. Magn.* **32**, 5085–5087 (1996).
- ⁹ A. Ghosh and P. Fischer, "Controlled propulsion of artificial magnetic nanostructured propellers," *Nano Lett.* **9**, 2243–2245 (2009).
- ¹⁰ L. Zhang, J. J. Abbott, L. Dong, K. E. Peyer, B. E. Kratochvil, H. Zhang, C. Bergeles, and B. J. Nelson, "Characterizing the swimming properties of artificial bacterial flagella," *Nano Lett.* **9**, 3663–3667 (2009).
- ¹¹ S. Tottori, L. Zhang, F. Qiu, K. K. Krawczyk, A. Franco-Obregón, and B. J. Nelson, "Magnetic helical micromachines: Fabrication, controlled swimming, and cargo transport," *Adv. Mater.* **24**, 811–816 (2012).
- ¹² S. Tottori, L. Zhang, K. E. Peyer, and B. J. Nelson, "Assembly, disassembly, and anomalous propulsion of microscopic helices," *Nano Lett.* **13**, 4263–4268 (2013).
- ¹³ K. E. Peyer, S. Tottori, F. Qiu, L. Zhang, and B. J. Nelson, "Magnetic helical micromachines," *Chem. Eur. J.* **19**, 28–38 (2013).
- ¹⁴ B. J. Nelson, I. K. Kaliakatsos, and J. J. Abbott, "Microrobots for minimally invasive medicine," *Annu. Rev. Biomed. Eng.* **12**, 55–85 (2010).
- ¹⁵ W. Gao, D. Kagan, O. S. Pak, C. Clawson, S. Campuzano, E. Chuluun-Erdene, E. Shipton, E. E. Fullerton, L. Zhang, E. Lauga *et al.*, "Cargo-towing fuel-free magnetic nanoswimmers for targeted drug delivery," *Small* **8**, 460–467 (2012).
- ¹⁶ J. Wang and W. Gao, "Nano/microscale motors: Biomedical opportunities and challenges," *ACS Nano* **6**, 5745–5751 (2012).
- ¹⁷ J. Lighthill, "Flagellar hydrodynamics - von Neumann lecture, 1975," *SIAM Rev.* **18**(2), 161–230 (1976).
- ¹⁸ E. Lauga and T. R. Powers, "The hydrodynamics of swimming microorganisms," *Rep. Prog. Phys.* **72**, 096601 (2009).
- ¹⁹ Z. Carvalho-Santos, J. Azimzadeh, J. B. Pereira-Leal, and M. Bettencourt-Dias, "Tracing the origins of centrioles, cilia, and flagella," *J. Cell Biol.* **194**, 165–175 (2011).
- ²⁰ E. M. Purcell, "Life at low Reynolds-number," *Am. J. Phys.* **45**(1), 3–11 (1977).
- ²¹ J. Gray and G. J. Hancock, "The propulsion of sea-urchin spermatozoa," *J. Exp. Biol.* **32**(4), 802–814 (1955).
- ²² S. Childress, *Mechanics of Swimming and Flying* (Cambridge University Press, Cambridge, UK, 1981), Vol. 2.

- ²³ B. Rodenborn, C.-H. Chen, H. L. Swinney, B. Liu, and H. P. Zhang, "Propulsion of microorganisms by a helical flagellum," *Proc. Natl. Acad. Sci. U.S.A.* **110**, E338–E347 (2013).
- ²⁴ M. Kim, J. C. Bird, A. J. Van Parys, K. S. Breuer, and T. R. Powers, "A macroscopic scale model of bacterial flagellar bundling," *Proc. Natl. Acad. Sci. U.S.A.* **100**, 15481–15485 (2003).
- ²⁵ M. Kim and T. R. Powers, "Hydrodynamic interactions between rotating helices," *Phys. Rev. E* **69**, 061910 (2004).
- ²⁶ M. Kim, M. Kim, J. C. Bird, J. Park, T. R. Powers, and K. S. Breuer, "Particle image velocimetry experiments on a macro-scale model for bacterial flagellar bundling," *Exp. Fluids* **37**, 782–788 (2004).
- ²⁷ M. Reichert and H. Stark, "Synchronization of rotating helices by hydrodynamic interactions," *Eur. Phys. J. E* **17**, 493–500 (2005).
- ²⁸ H. Flores, E. Lobaton, S. Méndez-Diez, S. Tlupova, and R. Cortez, "A study of bacterial flagellar bundling," *Bull. Math. Biol.* **67**, 137–168 (2005).
- ²⁹ P. J. A. Janssen and M. D. Graham, "Coexistence of tight and loose bundled states in a model of bacterial flagellar dynamics," *Phys. Rev. E* **84**, 011910 (2011).
- ³⁰ S. Lim and C. S. Peskin, "Fluid-mechanical interaction of flexible bacterial flagella by the immersed boundary method," *Phys. Rev. E* **85**, 036307 (2012).
- ³¹ S. Y. Reigh, R. G. Winkler, and G. Gompper, "Synchronization and bundling of anchored bacterial flagella," *Soft Matter* **8**, 4363–4372 (2012).
- ³² S. Y. Reigh, R. G. Winkler, and G. Gompper, "Synchronization, slippage, and unbundling of driven helical flagella," *PLoS ONE* **8**, e70868 (2013).
- ³³ H. C. Fu, T. R. Powers, and H. C. Wolgemuth, "Theory of swimming filaments in viscoelastic media," *Phys. Rev. Lett.* **99**, 258101–258105 (2007).
- ³⁴ A. M. Leshansky, "Enhanced low-Reynolds-number propulsion in heterogeneous viscous environments," *Phys. Rev. E* **80**, 051911 (2009).
- ³⁵ H. C. Fu, C. W. Wolgemuth, and T. R. Powers, "Swimming speeds of filaments in nonlinearly viscoelastic fluids," *Phys. Fluids* **21**, 033102 (2009).
- ³⁶ B. Liu, T. R. Powers, and K. S. Breuer, "Force-free swimming of a model helical flagellum in viscoelastic fluids," *Proc. Natl. Acad. Sci. U.S.A.* **108**, 19516–19520 (2011).
- ³⁷ S. E. Spagnolie, B. Liu, and T. Powers, "Locomotion of helical bodies in viscoelastic fluids: enhanced swimming at large helical amplitudes," *Phys. Rev. Lett.* **111**, 068101 (2013).
- ³⁸ J. J. L. Higdon, "The hydrodynamics of flagellar propulsion: Helical waves," *J. Fluid Mech.* **94**, 331–351 (1979).
- ³⁹ E. M. Purcell, "The efficiency of propulsion by a rotating flagellum," *Proc. Natl. Acad. Sci. U.S.A.* **94**, 11307–11311 (1997).
- ⁴⁰ N. Watari and R. G. Larson, "The hydrodynamics of a run-and-tumble bacterium propelled by polymorphic helical flagella," *Biophys. J.* **98**, 12–17 (2010).
- ⁴¹ S. E. Spagnolie and E. Lauga, "Comparative hydrodynamics of bacterial polymorphism," *Phys. Rev. Lett.* **106**, 058103 (2011).
- ⁴² B. Liu, K. S. Breuer, and T. R. Powers, "Propulsion by a helical flagellum in a capillary tube," *Phys. Fluids* **26**, 011701 (2014).
- ⁴³ S. Childress, "A thermodynamic efficiency for Stokesian swimming," *J. Fluid Mech.* **705**, 77–97 (2012).
- ⁴⁴ E. E. Keaveny and M. J. Shelley, "Hydrodynamic mobility of chiral colloidal aggregates," *Phys. Rev. E* **79**, 051405 (2009).
- ⁴⁵ E. E. Keaveny, S. Walker, and M. J. Shelley, "Optimization of chiral structures for microscale propulsion," *Nano Lett.* **13**, 531–537 (2013).
- ⁴⁶ K. I. Morozov and A. M. Leshansky, "The chiral magnetic nanomotors," *Nanoscale* **6**, 1580–1588 (2014).
- ⁴⁷ H. Power and G. Miranda, "Second kind integral equation formulation of Stokes flows past a particle of arbitrary shape," *SIAM J. Appl. Math.* **47**, 689–698 (1987).
- ⁴⁸ C. Pozrikidis, *Boundary Integral and Singularity Methods for Linearized Viscous Flow* (Cambridge University Press, Cambridge, UK, 1992).
- ⁴⁹ K. Atkinson and W. Han, *Theoretical Numerical Analysis* (Springer, New York, NY, 2009).
- ⁵⁰ K. E. Atkinson, *An Introduction to Numerical Analysis* (John Wiley & Sons, New York, 1978).
- ⁵¹ E. E. Keaveny and M. J. Shelley, "Applying a second-kind boundary integral equation for surface tractions in Stokes flow," *J. Comput. Phys.* **230**, 2141–2159 (2011).
- ⁵² A. A. Evans, S. E. Spagnolie, and E. Lauga, "Stokesian jellyfish: Viscous locomotion of bilayer vesicles," *Soft Matter* **6**, 1737–1747 (2010).
- ⁵³ B. Liu, K. S. Breuer, and T. R. Powers, "Helical swimming in Stokes flow using a novel boundary-element method," *Phys. Fluids* **25**, 061902 (2013).
- ⁵⁴ O. S. Pak, S. E. Spagnolie, and E. Lauga, "Hydrodynamics of the double-wave structure of insect spermatozoa flagella," *J. R. Soc. Interface* **9**, 1908–1924 (2012).
- ⁵⁵ S. Jung, K. Mareck, L. Fauci, and M. J. Shelley, "Rotational dynamics of a superhelix towed in a Stokes fluid," *Phys. Fluids* **19**, 103105 (2007).
- ⁵⁶ M. Sauzade, G. J. Elfring, and E. Lauga, "Taylor's swimming sheet: Analysis and improvement of the perturbation series," *Physica D* **240**, 1567–1573 (2011).
- ⁵⁷ C. M. Bender and S. A. Orszag, *Advanced Mathematical Methods for Scientists and Engineers I: Asymptotic Methods and Perturbation Theory* (Springer, 1999), Vol. 1.
- ⁵⁸ S. Childress, "Inertial swimmer as a singular perturbation," in *Proceedings of the ASME 2008 Dynamic Systems and Control Conference* (Ann Arbor, MI, USA, 2008).
- ⁵⁹ A. D. Stroock, S. K. W. Dertinger, A. Ajdari, I. Mezić, H. A. Stone, and G. M. Whitesides, "Chaotic mixer for microchannels," *Science* **295**, 647–651 (2002).

- ⁶⁰ A. D. Stroock, S. K. Dertinger, G. M. Whitesides, and A. Ajdari, "Patterning flows using grooved surfaces," *Anal. Chem.* **74**, 5306–5312 (2002).
- ⁶¹ S. Zhou, A. Sokolov, O. D. Lavrentovich, and I. S. Aranson, "Living liquid crystals," *Proc. Natl. Acad. Sci. U.S.A.* **111**, 1265–1270 (2014).
- ⁶² S. L. Tamm, "Ciliary motion in paramecium a scanning electron microscope study," *J. Cell Biol.* **55**, 250–255 (1972).
- ⁶³ K. Drescher, K. C. Leptos, I. Tuval, T. Ishikawa, T. J. Pedley, and R. E. Goldstein, "Dancing volvox: Hydrodynamic bound states of swimming algae," *Phys. Rev. Lett.* **102**, 168101 (2009).
- ⁶⁴ J. B. Waterbury, J. M. Willey, D. G. Franks, F. W. Valois, and S. W. Watson, "A cyanobacterium capable of swimming motility," *Science* **230**, 74–76 (1985).
- ⁶⁵ K. M. Ehlers, A. D. Samuel, H. C. Berg, and R. Montgomery, "Do cyanobacteria swim using traveling surface waves?," *Proc. Natl. Acad. Sci. U.S.A.* **93**(16), 8340–8343 (1996).
- ⁶⁶ H. A. Stone and A. D. T. Samuel, "Propulsion of microorganisms by surface distortions," *Phys. Rev. Lett.* **77**(19), 4102–4104 (1996).
- ⁶⁷ B. Brahmsha, "Non-flagellar swimming in marine *Synechococcus*," *J. Mol. Microbiol. Biotechnol.* **1**, 59–62 (1999).
- ⁶⁸ K. Ehlers and G. Oster, "On the mysterious propulsion of *Synechococcus*," *PloS ONE* **7**, e36081 (2012).